SUPPLEMENTARY MATERIAL

Detecting supraglacial debris thickness with GPR in suboptimal conditions

Alexandra GIESE, Steven ARCONE, Robert HAWLEY, Gabriel LEWIS, and Patrick WAGNON

Here, we provide more information on:

1. the methods for data collection (Figures S1 and S2)
2. a technical discussion of the response of a waveform to supraglacial debris, accompanied by Figures S3 and S4, and Figures S5 and S6 showing the Hilbert-transformed data only, without thickness measurements or radar-based thickness retrievals
3. a collection of four radargrams associated with each of the four rock box experimental configurations (S7 to S10)
4. a visual depiction (via photographs, Figures S11 to S21) of Changri Nup's supraglacial debris layer on each of the 5 transects profiled

Datasets detailing data collection and summarizing the thickness retrievals calculated from the leave-one-out cross validation (LOOCV)-derived thresholds are described here and available at https://glacioclim.osug.fr/Radar-data-on-Changri-Nup-Glacier. Radar data from the 2015 field season (in 7 .dzt files) is also available at https://glacioclim.osug.fr/Radar-data-on-Changri-Nup-Glacier. Code for calculating the threshold (xval_cng.m) and applying the threshold to calculate thickness retrievals (scale_cng.m) are available on the corresponding author's GitHub page (github.com/alexandragiese/GPR_loocv). A MATLAB script for reading .dzt RADAN files is available by request to Robert Hawley <robert.l.hawley@dartmouth.edu>

Data Set S1. The locations and directions of all GPR files recorded along the 5 transects A, B, C, D, and E, given by waypoint names.
Data Set S2. The coordinates of the waypoints named in Data Set 1.
Data Set S3. Field measurements of debris thickness on Changri Nup Glacier.
Data Set S4. Debris thickness retrievals (m) every m (transects A, B, C) or every dm (transects D, E), calculated via the LOOCV-derived threshold method presented in this study.

FURTHER DETAILS ON COLLECTED FIELD DATA

The various subplots of Figure S1 are zoomed-in sections from the top 1.5 m of Figure 4. These close-ups highlight some of the features and details which are not visible in the full radargram. Specifically, arrows within each detail indicate clear hyperbolic diffraction apices and faint hyperbolic asymptotes, caused by the elevation of the antenna. The white-black-white (+ - +) and black-white-black sequences indicate coherent wavelets. These subsurface responses are most likely caused by localized facets, rather than "point" targets. The columnar alignment of many events result from resonances and from multiple scattering within clumps of rock or slabs. Multiple scattering would explain why some events within a single column are not evenly spaced. Some of these longer streaks do not necessarily represent deep penetration.
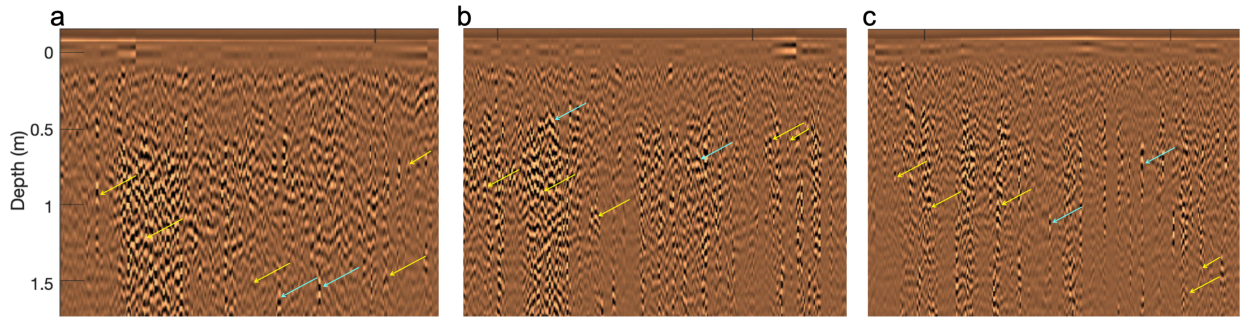
Fig. S1. Details extracted from the 75-m-radargram in Figure 4. The yellow arrows indicate a few of the myriad diffractions, each with weak asymptotes that fall off rapidly and are of weak amplitude because of the antenna elevation. The turquoise arrows in (a) and (c) indicate apices of diffractions comprised of a coherent wavelet but in (b) indicate meter scale coherent reflections.

Figure S2 shows the method of data collection in the field, with the operator adjacent to the elevated antenna unit. No interference from body reflections was present in the data.
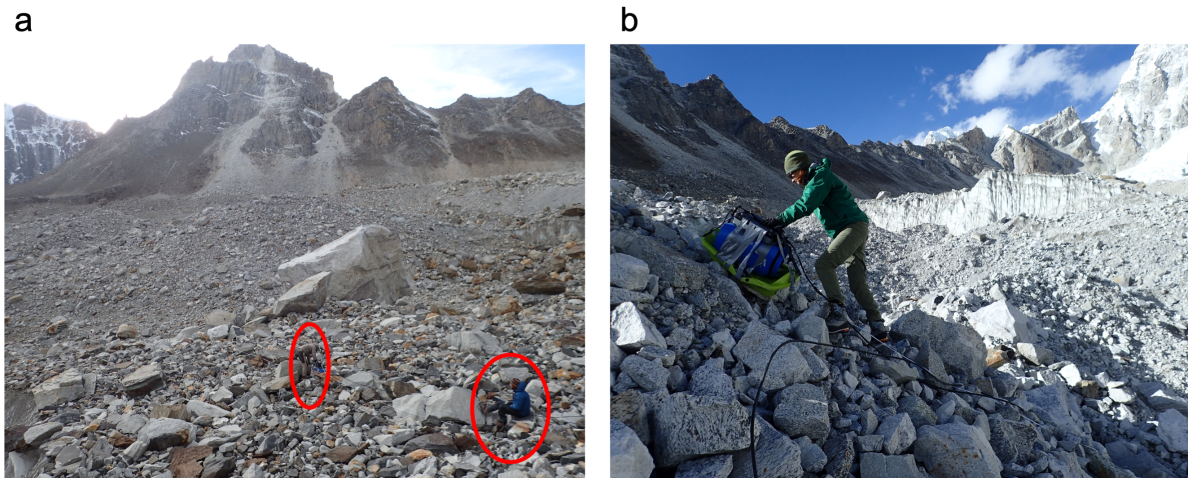

Fig. S2. Antenna unit operator, shown collecting data on (a) transect A with a 19-cm-elevated antenna unit and (b) transect B, which was the steepest, with a 27-cm-elevated antenna unit.
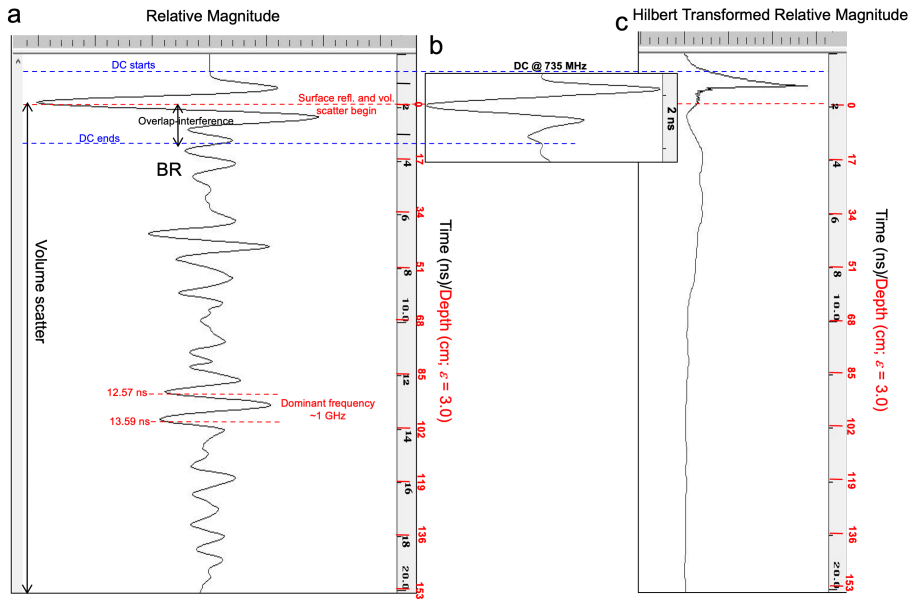
Fig. S3. The top 40% of a trace from 341 m along transect B of Changri Nup Glacier, showing wave characteristics. Panel (a): The trace with no processing, corrected only for time zero. The start and end of the direct coupling (DC) is indicated by the blue dashed lines, and the red dashed line indicates when surface reflection and volume scatter begin. The approximate depth and time of the debris bottom reflection (BR) is also labeled. Panel (b): Form and duration of only the DC at the same time scale (i.e., y-axis) as in (a). Panel (c): The trace from (a) with all processing applied: 10-fold stacking, background removal, deconvolution, geometric spreading correction, and Hilbert magnitude transformation.

GPR WAVEFORM RESPONSE TO SUPRAGLACIAL DEBRIS

In this section, we illustrate the details of the GPR waveform response while in the debris and while passing the debris-ice interface. Figure S3 shows a sample trace from transect B with various events labeled and also shows that same trace after Hilbert magnitude transformation. Of particular importance is the overlap of the direct coupling (DC) and the surface reflection. The depth scale for all panels is based on $\epsilon = 3$, as derived from the experiments in this study.

Panel (a) shows the trace with no processing, corrected only for time zero. Labels and dashed lines of corresponding colors show durations of the DC, surface reflection, and volume scatter. The DC and debris surface reflections overlap and, therefore, interfere. Note the lack of adjusted range gain greatly exaggerates signals at depths greater than ∼30 cm.

Panel (b) shows the form and duration of only the DC (without an interfering surface reflection) at the same time scale as in (a). This DC signal is what we attempt to remove with the background removal filter in panel (c).

Panel (c) shows the trace from (a) with processing of: 10-fold stacking, background removal, deconvolution, geometric spreading correction, and Hilbert magnitude transformation. We started the background removal at 1.27 ns, eliminating most of the subsequent superposition of the DC and surface reflection. Although volume scatter separates from the surface reflections at 3.4 ns, it technically starts at 1.9 ns, as soon as the wave enters the debris. The range gain correction, which accounts for geometric spreading loss, has reduced trace amplitudes. (Note that antenna unit height on the transect B profile was 27 cm. For the 19 cm height used on the other 4 transects, the surface reflection lasts from 1.33 ns – 2.83 ns, and the volume scatter arrives at 1.33 ns.)
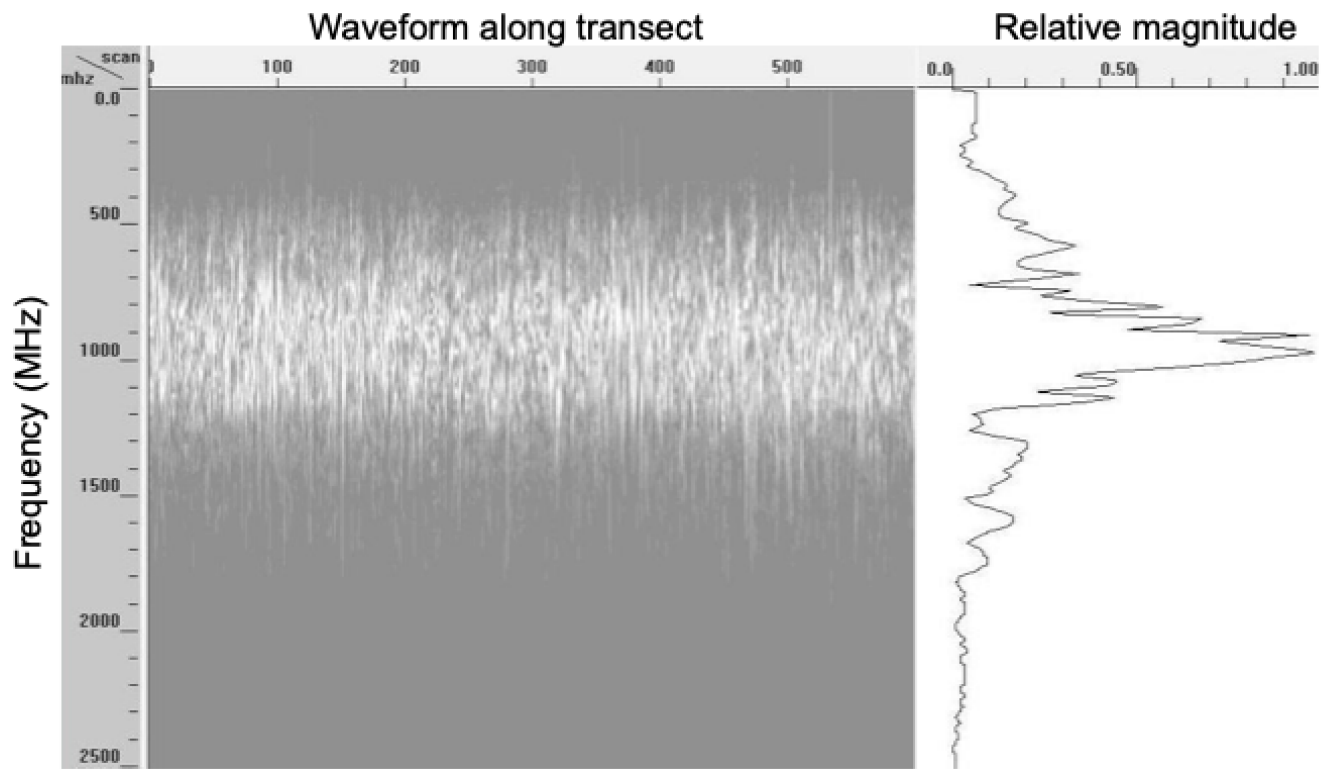
Fig. S4. Reflected pulse spectra for transect B, with the DC eliminated but before Hilbert transformation. In our rock box experiments, for the large clasts (max size 18 cm, roughly equivalent to an *in situ* wavelength), 960 MHz dropped to about 800 MHz. For the smallest clasts, it stayed near 1 GHz.

Typical returned pulse spectra are centered between $900 - 1000$ MHz and are shown in Figure S4. It is evident that the subsurface volume scatter is centered near the transmitted dominant frequency of 960 MHz.
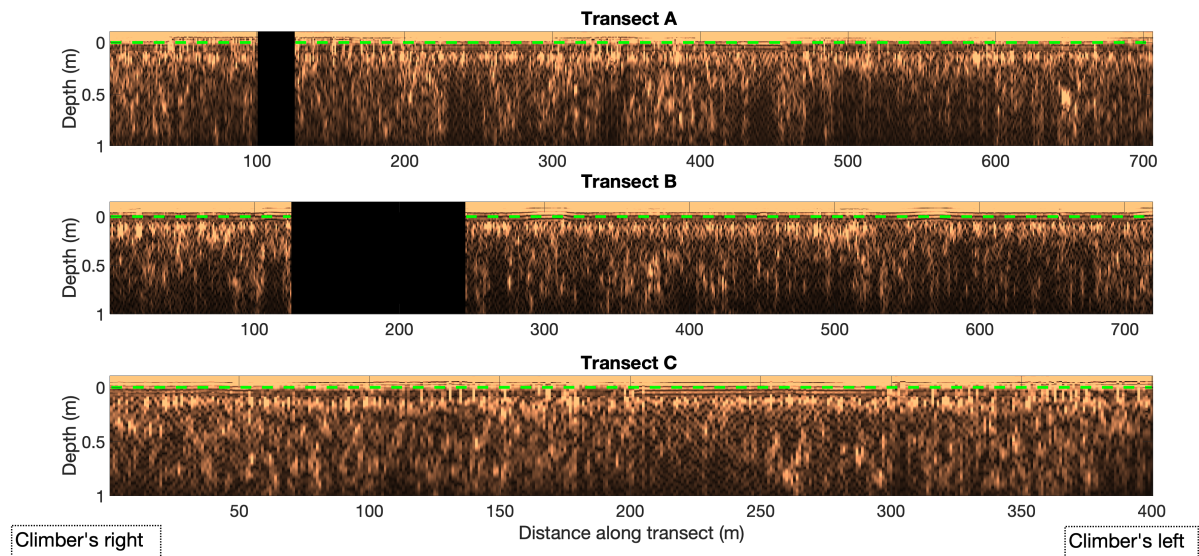
Fig. S5. Top 1 m of the Hilbert-transformed and 10x stacked GPR data collected along across-glacier transects A – C without the thickness measurements or radar-based thickness retrievals overlaid in Figure 5. All three run from climber's right to climber's left across the glacier; the 25 m gap in A indicates a corrupted file, and the 120 m gap in B is colocated with the prominent ice sail. The y-axis depth scale was calculated using $\epsilon = 3$, and 0 m is the debris surface. Note that the antenna unit was 8 cm higher over transect B. z is thickness, and minimum measured z is above frozen debris that prevented digging to the ice surface.
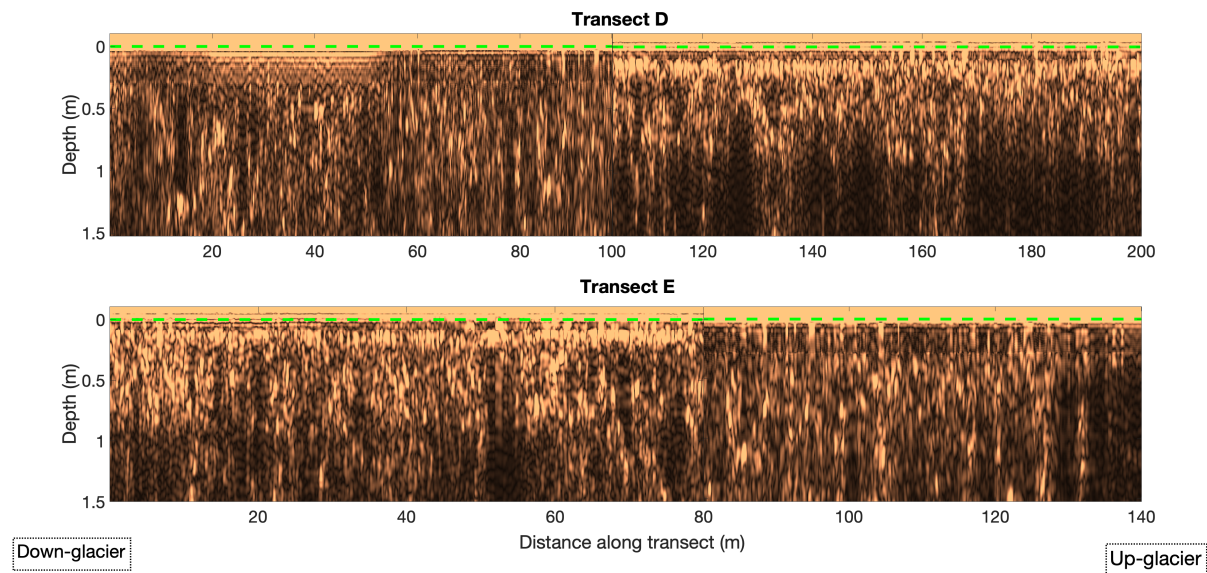

Fig. S6. Top 1.5 m of the Hilbert-transformed data collected on along-glacier transects D and E, starting at their down-glacier ends, without the thickness measurements or radar-based thickness retrievals overlaid in Figure 6. These profiles are much shorter than those in Figure S5 and, for visual interpretation, are not stacked here. As in Figure S5, z is thickness, and a depth of 0 m is the debris surface.

DATA FROM ROCK BOX EXPERIMENTS

In this section, we show the radargrams associated with the four experiments: with and without aluminum foil at the bottom of the rocky debris, profiled with 960 MHz and 2.6 GHz GPR. Antenna heights are noted in the figure captions. Figure S7 is Figure 7a, shown here again for completeness. Note that, as discussed in the manuscript, the 960 MHz signal penetrated the debris through all clast sizes. However, the 2.6 GHz signal's 6.7 cm *in situ* wavelength had difficulty penetrating medium and large clasts. The only visible returns from the foil layer are beneath the smaller clasts.
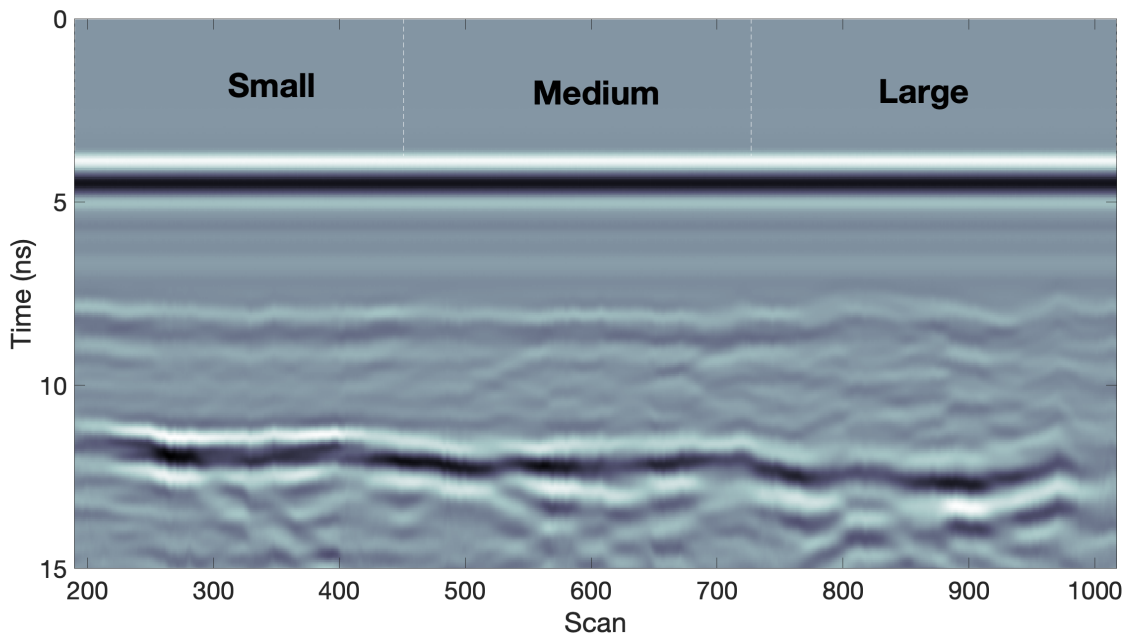

Fig. S7. A radar profile collected with a raised 960 MHz antenna unit over the rock box in Figure 3 that had three partitioned clast size sections, under which aluminum foil provided a strong bottom reflection. Total debris depths were 28.6 cm, 29.6 cm, and 33.6 cm over the small debris, medium debris, and large debris sections, respectively. The antenna was raised 60 cm.
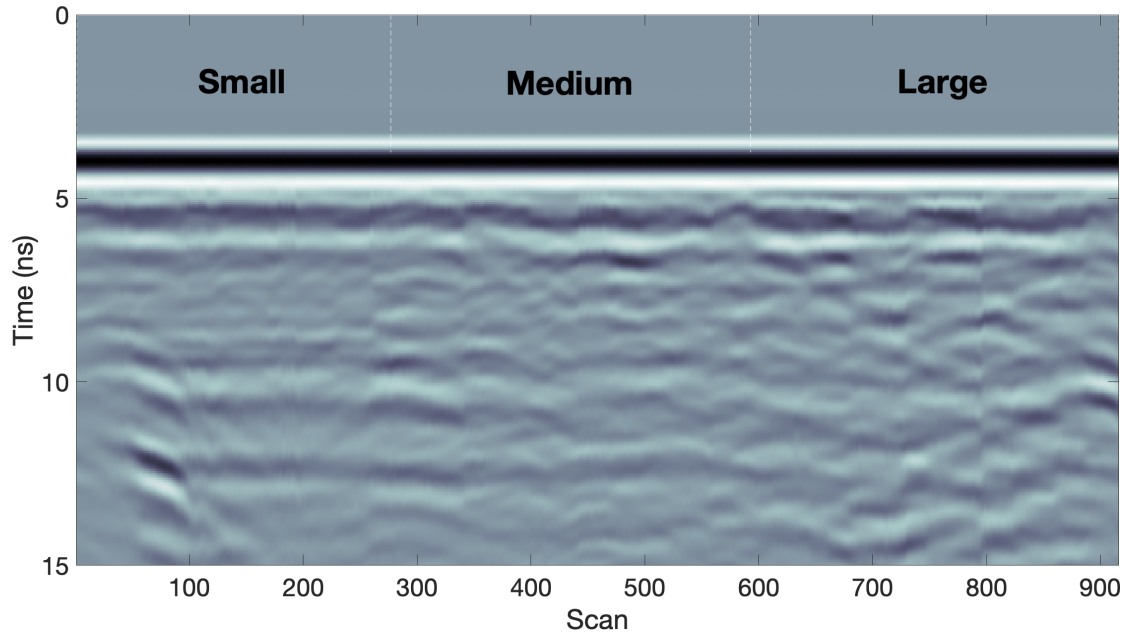
Fig. S8. A radar profile collected with a raised 960 MHz antenna unit over the rock box in Figure 3 that had three partitioned clast size sections. Lack of dielectric contrast between the debris and the pine bale substrate explains the absence of a detectable interface at the bottom of the debris. The antenna was raised 20 cm.
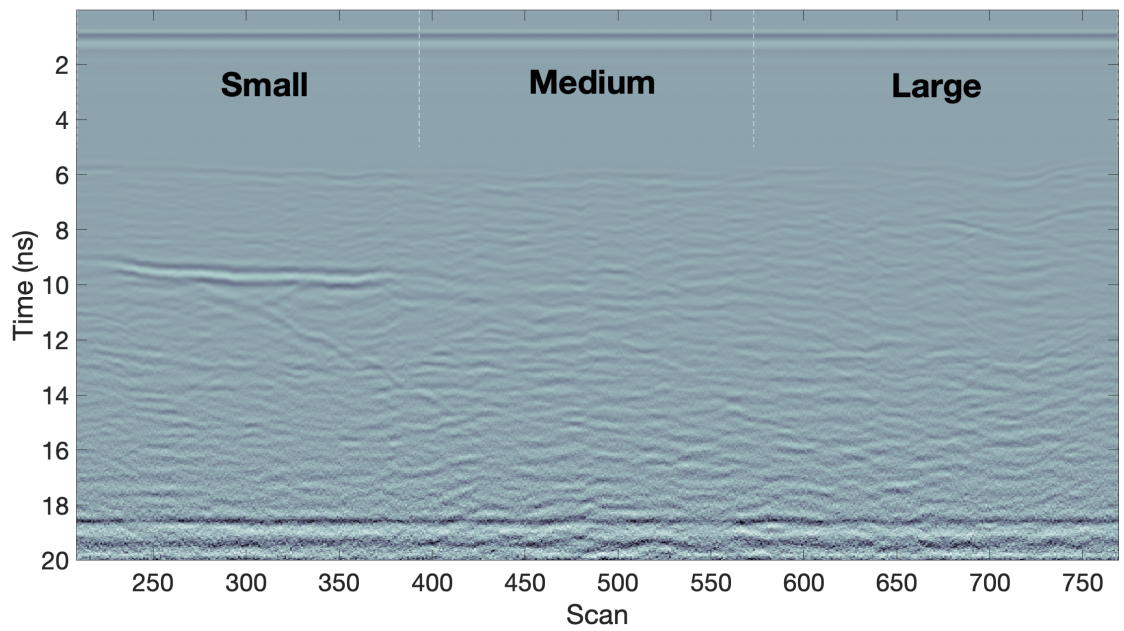

Fig. S9. A radar profile collected with a raised 2.6 GHz antenna unit over the rock box in Figure 3 that had three partitioned clast size sections, under which aluminum foil provided a strong bottom reflection. Total debris depths were 28.6 cm, 29.6 cm, and 33.6 cm over the small debris, medium debris, and large debris sections, respectively. The antenna was raised 60 cm.
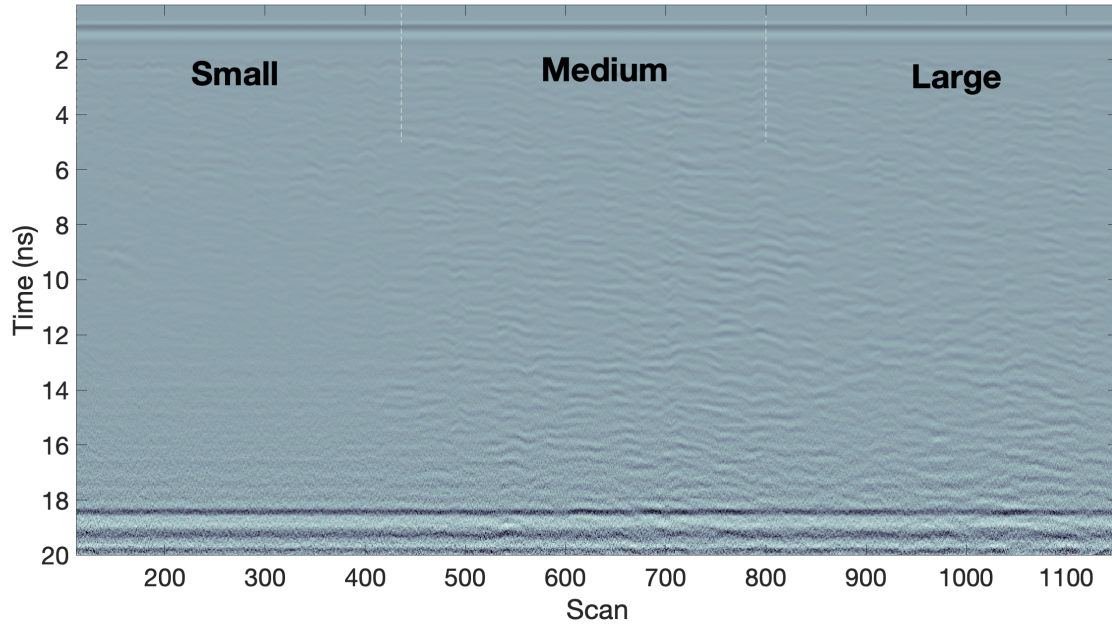
Fig. S10. A radar profile collected with a raised 2.6 GHz antenna unit over the rock box in Figure 3 that had three partitioned clast size sections. Lack of dielectric contrast between the debris and the pine bale substrate explains the absence of a detectable interface at the bottom of the debris. The antenna was raised 20 cm.

PHOTOS BY TRANSECT

Here we include photos of each transect for depiction of the debris we profiled. Each photo shows typical debris surface roughness and clast sizes. In most photos, GPR operators or other objects (e.g., tape measure) provide scale.

Fig. S11. Photograph 1/2 of transect A. Note the thin debris cover over mostly clear ice. Some parts of transects went along cliffs edges such as this one; others went up and over similar features.

Fig. S12. Photograph 2/2 of transect A. Exposed ice is visible to the left; note two field workers for scale in middle right.

Fig. S13. Photograph 1/3 of transect B. Note significant clast size variability.

Fig. S14. Photograph 2/3 of transect B.

Fig. S15. Photograph 3/3 of transect B. In spite of the large-scale roughness, the debris cover continued to be relatively shallow.

Fig. S16. Photograph 1/2 of transect C. Note extreme terrain.

Fig. S17. Photograph 2/2 of transect C. Note duffel bag for scale at left.

Fig. S18. Photograph 1/2 of transect D.

Fig. S19. Photograph 2/2 of transect D.

Fig. S20. Photograph 1/2 of transect E.

Fig. S21. Photograph 2/2 of transect E. Note englacial melt-out occurring.